RICE UNIVERSITY

Curvature Effects on the Optical Transitions of Single-Wall Carbon Nanotubes

by

Erik H. Hároz

A Thesis Submitted
in Partial Fulfillment of the
Requirements for the Degree

Master of Science

Approved, Thesis Committee:

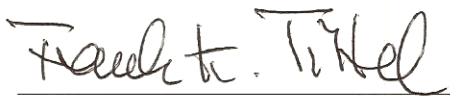

Frank K. Tittel, Chair
J. S. Abercrombie Professor of Electrical and Computer Engineering

Qianfan Xu
Assistant Professor of Electrical and Computer Engineering

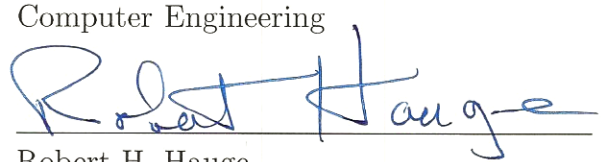

Robert H. Hauge
Distinguished Faculty Fellow of Chemistry

Houston, Texas

November, 2012

ABSTRACT

Curvature Effects on the Optical Transitions of Single-Wall Carbon Nanotubes

by

Erik H. Hároz

Optical transition energies are widely used for providing experimental insight into the electronic band structure of single-wall carbon nanotubes (SWCNTs). While the first and second optical transitions in semiconducting carbon nanotubes have already been heavily studied, due to experimental difficulties in accessing the relevant excitation energy region, little is known about higher lying transitions. Here, I present measurements of the third and fourth optical transitions of small-diameter (0.7-1.2 nm), semiconducting single-wall carbon nanotubes via resonant Raman spectroscopy in the visible deep blue region (415-465 nm) and photoluminescence excitation spectroscopy in the ultraviolet and visible blue optical regions (280-488 nm). Diameter-dependent Raman radial breathing mode features, as well as resonant energy excitation maxima determined by Raman and photoluminescence measurements, are assigned to specific (n, m) nanotube species. The Raman intensity within a given $2n+m$ branch is found to increase with decreasing chiral angle, consistent with similar measurements for lower order optical states. Additionally, increased excitation line widths and weaker Raman intensities are observed as higher lying transitions are accessed for a given nanotube, in agreement with previous Raman measurements. Chiefly, a scaling law analysis that removes the chiral-angle-dependent contribution to the optical transition energy indicates that the third and fourth transition energies ex-

hibit a significant deviation from the energy trend line observed for the first and second optical transitions, when the transition energies are plotted as a function of nanotube diameter. This deviation can be understood in the context of a change in the competition between exchange and excitonic correction terms. Furthermore, for semiconducting SWCNTs with diameters less than 0.9 nm, an additional deviation is observed that is interpreted as the first observation of crossing-over of the third and fourth transition energy trend lines for a given $2n+m$ branch and a chirality dependence in the many-body excitonic effects that becomes significant at high nanotube curvatures.

Acknowledgments

I would like to thank Prof. Frank Tittel, Prof. Qianfan Xu, and Dr. Robert Hauge, for agreeing to serve on my thesis committee; my colleagues, Dr. Stephen Doorn, Prof. Bruce Weisman, and Dr. Sergei Bachilo, for contributing to this work; my parents, Hector and Carolina, for always encouraging me to follow my dreams; my children, Olivia and James, for making my life full of happiness and laughter; and most importantly, my wife, Ellaine, for her unending love and support through all these years.

This thesis is dedicated in loving memory to my godfather, Hector Hároz; my mother-in-law, Linda Galbizo; my maternal grandparents, Jaime and Rosa Torres; and most importantly my mother, Maruja Hároz, who always believed in me, gave me a love of learning and has watched over me all these years.

Contents

Illustrations

Tables

Chapter 1

Introduction

1.1 Motivation

Optical transition energies are one of the most widely used physical properties measured for providing experimental insight into the electronic band structure of single-wall carbon nanotubes (SWCNTs). With advances in photoluminescence excitation (PLE) and resonant Raman scattering (RRS) spectroscopies, researchers have definitively assigned the electronic and vibrational spectral features of SWCNTs to their corresponding nanotube chiralities. These assignments are facilitated by the occurrence of patterns that group the PLE [7] or Raman radial breathing mode (RBM) [8–11] spectral features according to similar $2n+m$ branches or "families", where n and m are the chiral indices which define the diameter and chiral angle of a given nanotube. Individual features may then be paired unambiguously with their corresponding nanotube structural indices (n, m). These assignments have led to the development of useful semi-empirical formulas for calculation of E_{11} and E_{22} transition energies for both semiconducting [7, 11, 12] and metallic [11, 13] nanotube types. Experimentally based plots of optical transition energy as a function of nanotube diameter, the so-called Kataura plot [14], or RBM frequency have also resulted [2,9,12,15].

Such accurate assignments and development of the experimentally-based Kataura plots are of great utility for characterizing nanotube sample composition and are important aids for development of methods for selective synthesis, understanding of

selective reaction chemistry and separations, as well as for understanding chirality-dependent effects on a variety of nanotube photophysical behaviors. The experimental energies and Kataura plots have guided theoretical efforts at describing energies and electronic structure based on an excitonic description [3, 16–22]. Incorporation of the relevant many-body effects into an extended tight binding description of nanotube electronic structure now yields good agreement with observed E_{11} and E_{22} values [1,3].

Extending optical studies into the higher lying E_{33} and E_{44} transitions is of interest for both theoretical and applied reasons. This is an important excitation region for sample characterization via Raman, since commonly used visible excitation lines (e.g. 532, 514, and 488 nm) are capable of accessing this region, particularly for the larger diameter nanotubes generated by chemical vapor deposition [23,24], laser-oven [25,26], and vertical-array [27, 28] growth methods commonly used for producing nanotubes for a wide range of electronics and materials applications. To better understand the electronic, optical, and materials properties of such nanotubes, it is necessary to correlate their behaviors to structure. This requires accurate Kataura plots covering the E_{33} and E_{44} transition regions, similar to those now available for the lower lying E_{11} and E_{22} transitions. Analogously to the lower energy transitions, it will also be important to determine if accurate semi-empirical, or even first-principles analytical expressions, can be developed for facile assignment of spectroscopic features in PLE and RBM spectra. From a more fundamental standpoint, expanded studies of the E_{33} and E_{44} region are necessary for developing a more complete understanding of underlying electronic structure at higher energies. Such studies, for example, will allow the assessment of whether or not trends observed in excitonic behavior and exciton-phonon coupling continue at higher energies.

Recent resonant Raman work by Araujo et al. [2] has probed the E_{33} and E_{44}

transitions for a large number of nanotube chiralities in the 1.1 to 2.3 nm diameter range. The observed transition energies were described in terms of a nonlinear scaling law analysis that accounts for many-body exciton effects [1, 17, 20]. It was demonstrated that distinctly different behavior is observed for the E_{33} and E_{44} transitions, in comparison to those for E_{11} and E_{22} [2]. Similar results on a small set of index-identified single nanotubes in the diameter range of 1.4 to 2.4 nm have been reported as well [29]. The $1/d_t$ dependence observed in the deviation between the higher and lower transitions points to a change in excitonic behavior at higher energies. The results of Araujo and coworkers have produced new physical insight into the behavior of the higher lying transitions in carbon nanotubes, with these results ultimately demonstrating that the E_{33} and E_{44} transitions cannot be described by simple extensions of E_{11} and E_{22} patterns. Additionally, those results have shown that the nonlinear scaling laws can be used as an accurate basis for calculating Kataura plots useful for identifying spectral features at these higher energies.

It remains an open question, however, whether or not the large diameter E_{33} and E_{44} scaling-law behavior holds for smaller diameter nanotubes. In general, such highly curved nanotubes are known to display unique behaviors not observed for large diameters. For example, trigonal warping and curvature effects on observed transition energies become much more pronounced at smaller diameters [30, 31]. RBM frequencies also begin to show deviations from expected trends near the small-diameter limit [1, 8, 32]. It is therefore important to probe how E_{33} and E_{44} respond at small diameters as well.

1.2 Outline

Here, I present measurements of the third and fourth (E_{33}^S and E_{44}^S, respectively) optical transitions of small-diameter (0.71.2 nm), semiconducting single-wall carbon nanotubes via resonant Raman spectroscopy in the visible deep blue region (415-465 nm) and photoluminescence excitation spectroscopy in the ultraviolet and visible blue optical regions (280-488 nm). In chapter 2 of this thesis, I briefly describe the experimental setup used to perform the aforementioned RRS and PLE measurements as well as the centrifugation method used to produce the aqueous SWCNT suspension studied. In chapter 3, I present the optical spectra obtained in these experiments. Diameter-dependent radial breathing mode features, as well as Raman and photoluminescence excitation maxima, are assigned to specific nanotube species. The Raman intensity within a given $2n+m$ branch is found to increase with decreasing chiral angle, consistent with similar measurements for lower order optical states, as does the trend toward increased excitation line widths and weaker Raman intensities as higher lying transitions are accessed. In chapter 4, using a scaling law fit that removes the chiral angle-dependent term to the optical transition energy, the third and fourth transition energies are shown to exhibit a significant deviation from the trend line observed for the first and second (E_{11}^S and E_{22}^S, respectively) optical transitions, when plotted as a function of nanotube diameter. This deviation can be understood in the context of a change in the competition between exchange and excitonic correction terms. Furthermore, for semiconducting SWCNTs with diameters less than 0.9 nm, an additional deviation is observed that is interpreted as the first observation of crossing-over of the third and fourth transition energy trend lines for a given $2n+m$ branch and a chirality dependence in the many-body exciton effects that becomes significant at high curvatures. Finally, in chapter 5, we summarize the main accomplishments of

this work and suggest future areas of investigation.

The contents of this thesis are taken in large part from the first-author work of Hároz *et al.* [4].

Chapter 2

Experimental Methods

2.1 Nanotube Sample

To observe the distinct optical transitions for each specific chirality present in an ensemble sample of single-wall carbon nanotubes (SWCNTs), SWCNTs were required to be dispersed as individual molecules to remove the effect of intertube interactions on the nanotube electronic band structure. To that end, a variation of the standard ultracentrifugation technique first developed by O'Connell *et al.* [33] was employed to produce a "homogeneous" sample. Pristine, single-walled carbon nanotubes (SWCNTs) were synthesized by the high-pressure carbon monoxide (HiPco) method at Rice University. As-produced HiPco SWCNTs (batch HPR 120.5) were initially dispersed in 1% (wt./vol.) sodium dodecyl sulfate (SDS) in deuterated water by bath sonication (Cole-Parmer 60 W ultrasonic cleaner, model #08849-00) for 30 minutes, using a starting SWCNT concentration of 200 mg/L. The suspension was then further sonicated by probe ultrasonicator (Cole-Parmer 500 W ultrasonic processor, model #CPX-600, 0.25 inch probe, 35% amplitude) for 60 minutes while being cooled in a water bath maintained at 10°C. Finally, the suspension was centrifuged for 4 hours at 109,500 g average (Sorvall Discovery 100SE Ultracentrifuge using a Sorvall AH-629 swing bucket rotor). After centrifugation, the upper 60% of the supernatant was removed and used for optical measurements.

2.2 Resonant Raman Scattering

Resonant Raman spectroscopy (RRS) was performed in a backscattering configuration with tunable dye laser excitation using stilbene dye scanned from 465 to 415 nm (2.67-2.99 eV) in 2 nm steps. Excitation power was maintained at 25 mW. Individual Stokes-shift spectra were obtained as 5 min integrations using a charge coupled device mounted on a SPEX triple monochromator. The frequency of each carbon nanotube spectrum was calibrated at each excitation wavelength with the nonresonant Raman spectrum of carbon tetrachloride (CCl_4). Intensities were corrected for instrument response and $\omega^4_{scattered}$-dependence using a calibration curve obtained by fitting the intensity of the 218.6 and 314.2 cm^{-1} Raman peaks of CCl_4 as a function of excitation wavelength with a third-order polynomial function. All Raman spectra were taken at room temperature and ambient pressure.

2.3 Photoluminescence Excitation Spectroscopy

Two-dimensional (2D) excitation-emission spectra of photoluminescence were acquired on a Fluorolog-3-211 (HORIBA Jobin-Yvon). Excitation light with a 5 nm bandwidth in the wavelength range from 280 to 480 nm (4.43-2.58 eV) was obtained from a Xe lamp using a double monochromator. Nanotube emission was measured from 900 to 1550 nm with a single-channel cooled InGaAs detector via a monochromator with 6 nm bandpass. Spectra were acquired with 2 nm steps in both excitation and emission wavelengths. Individual spectra were acquired with 1 s per point integration times and were repeated, as required, to ensure reproducibility and to improve signal to noise ratio. The detectors were calibrated with a reference lamp for quantum value (quanta per spectral range/nm), not power. The excitation refer-

ence sensor/photodiode is also calibrated relatively with the excitation spectra of the known absorption for that sample at that particular excitation energy. The spectral signal from the detector (voltage or counting) is multiplied by a correcting spectrum for it to represent the shape of a quantum spectrum and divided by the signal from the reference detector in the excitation channel, which is also multiplied by its correcting spectrum.

Chapter 3

Results

3.1 Resonant Raman Scattering Spectra

Raman spectra representative of those obtained across the excitation range are shown in Figure 3.1 for the radial breathing mode (RBM) region of the spectrum. Spectra show the oscillatory behavior observed at lower excitation energies, for which features from different $2n+m$ = constant branches grow in intensity and then decay sequentially as excitation energy is varied. Two main $2n+m$ branches are observed in the data, centered at ≈ 225 cm^{-1} and 250 cm^{-1}. Additional features not associated with these two main groupings are also observed, particularly at lower excitation energies. Assignment of these features to specific chiralities requires correlation of RBM frequencies to excitation energies and matching of the resultant branching patterns to theoretical expectations.

Spectral patterns arising from correlations of transition energy to nanotube diameter or RBM frequency have been instrumental in assignment of spectral features to specific (n, m) designations [2, 11]. For example, RBM features belonging to nanotubes of the same $2n+m$ = constant branches show hooked energy spread branching patterns resulting from deviations of observed transition energies from an idealized tight binding description of armchair energies. As one progresses from the near-armchair chiralities to near-zigzag chiralities within a given $2n+m$ branch, these deviations increase, resulting in the familiar pattern. Such patterns are readily observed

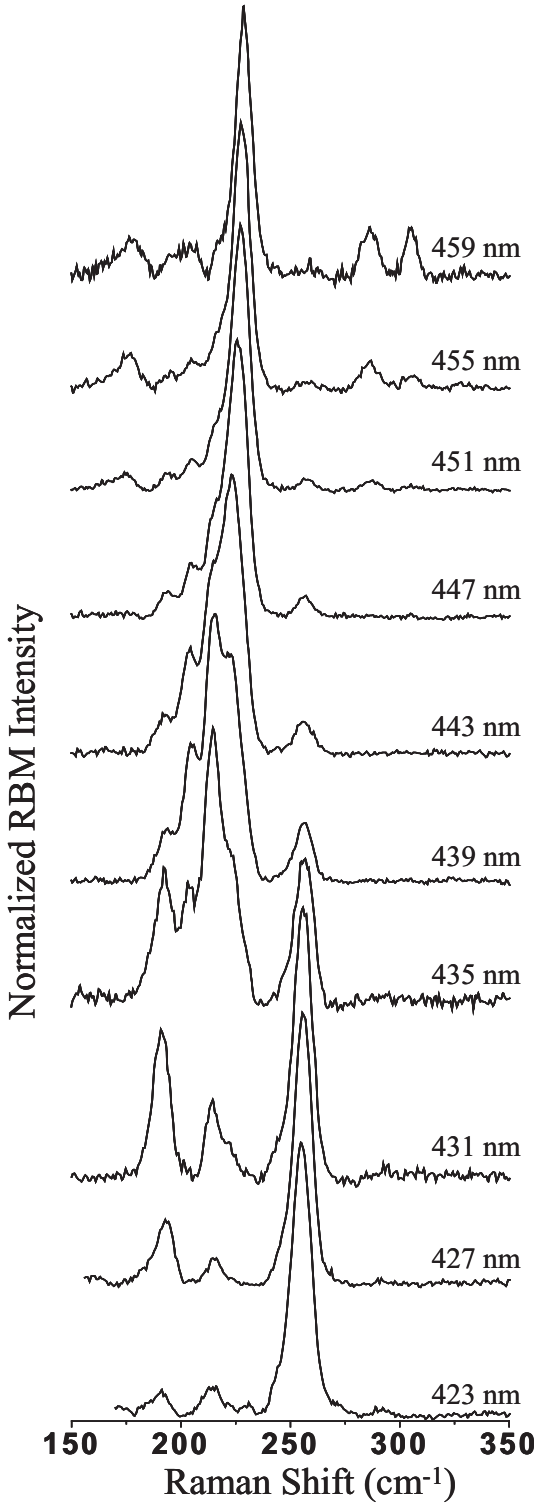

Figure 3.1 : Representative carbon nanotube Raman RBM spectra for different excitation wavelengths. The main features appear in two clusters of RBM parks corresponding to SWCNTs belonging to two particular $2n+m$ branches. For clarity, individual spectral intensities are normalized with respect to the most intense peak in each spectrum.

when RBM frequencies are plotted against excitation energy in a two-dimensional intensity map and permit grouping readily of individual features by branch. Such a plot is shown in Figure 3.2(a) for the Raman data. Figure 3.2(a) allows one to conclude, for example, that the RBM features between 204 and 230 cm^{-1}, in the excitation region of 2.7 to 2.85 eV, belong to a single $2n+m$ branch. Another branch is clearly delineated in the frequency range of 230 to 256 cm^{-1}, for excitation energies ranging from about 2.85 to 3 eV.

The strategy for assignment of the observed RBM features to specific (n, m) designations is first to compare the experimental Kataura plot results of Figure 3.2(a) to features expected from an Extended Tight Binding (ETB) model [34] that incorporates many-body effects resulting from exciton formation [1, 3, 22]. Excellent agreement has been demonstrated by Jorio *et al.* between the ETB model and E_{11} and E_{22} transition energies [1]. Patterns are correlated between the two plots to assign chiralities. In the event that multiple plausible choices, or overlapping of similar patterns exist for specific RBM features, assignments will be made via reference to other features occurring in the spectra to produce a globally consistent comparison. Such an approach works best when complete $2n+m$ branches are present for comparison. Thus, the two main branches that are observed are assigned first and then used to anchor the spectral behavior for identification of the remaining features that are not clearly linked to other branches (for example, the lone RBM feature occurring at 193 cm^{-1} and centered at excitation energy near 2.86 eV).

As a reference point for to the assignments made here, a detail of the ETB results for the region centered around the Raman excitation energies is shown in Figure 3.2(b). Features found in this plot belong primarily to E_{11}^M and E_{33}^S, (both mod $(n-m, 3) = 1$ and 2 types, referred to hereafter as mod1 and mod2, respectively)

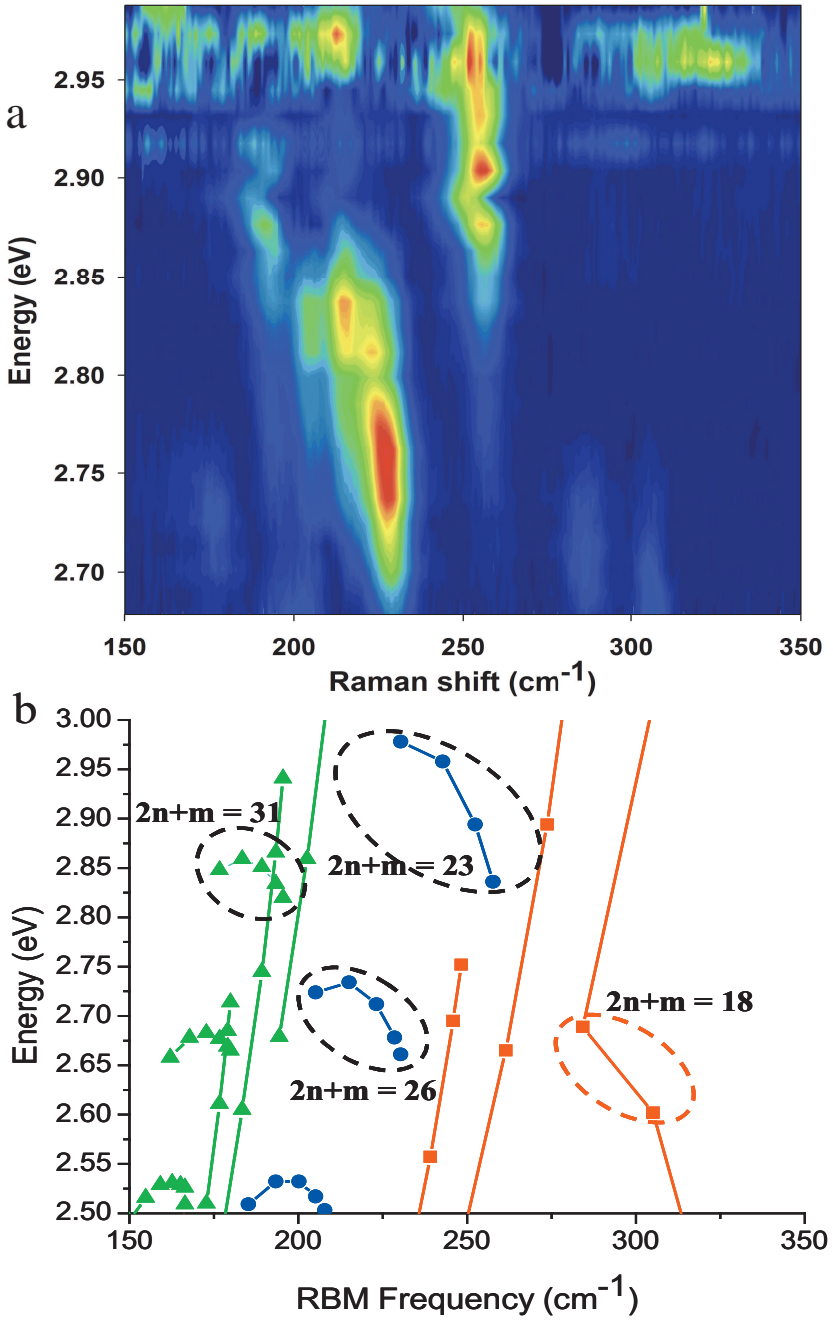

Figure 3.2 : a) 2D contour plot showing RBM intensity behavior as a function of excitation energy and RBM frequency. The contour plot shows grouping of the main RBM features into $2n+m =$ constant branches. b) A plot of optical transition energies calculated using the ETB method versus RBM frequency [1] predicted 16 features within the same energy/RBM frequency region for mod 2 semiconductors (E_{33} and E_{44}, green triangles), mod 1 semiconductors (E_{33}, blue circles), and metallics (E_{11}, red squares). The highlighted branches correspond to the observed features in part (a) and in Fig. 3.1.

and E_{44}^S (mod 2 type) transitions, where M and S refer to metallic and semiconducting species, respectively. Two branches (corresponding to E_{33}^S transitions for $2n+m$ = 23 and 26) that appear in the ETB plot (Figure 3.2(b), highlighted by dashed ellipses) are good candidates for the features observed in the experimental data. Although the transition energies do not match, they are the only features in the ETB plot with RBM frequencies that are well-matched to the experimental frequencies. Additionally, the two branches are separated in energy by the same relative amounts as the branches appearing in the ETB plot. Thus, I assign the two branches centered at RBM frequencies of 225 and 250 cm^{-1} to $2n+m$ = 23 and 26, respectively. The higher frequency RBMs in each branch correspond to the near-zigzag chiralities, allowing final assignment of individual RBMs to specific chiralities as shown in Table 3.1. The blueshift in E_{33}^S transition energies from ETB expectations is consistent with behavior previously observed [2] and is discussed below.

The RBMs found at 286 cm^{-1} and 305 cm^{-1} with lower energy excitation (451 nm to 463 nm, see Fig. 3.1, are assigned to the features circled in red in Figure 3.2(b). The observed frequencies are an excellent match and, although I was unable to complete the excitation profiles on the low energy side for these species because of the limited excitation range of the stilbene laser dye, the energy range over which we observe them is in good agreement with the ETB-based Kataura plot (as expected for E_{11}^M , see ref. [2]). These features are therefore assigned as the (6,6) and (7,4) nanotubes of the $2n+m$ = 18 branch. This assignment is also consistent with previous resonance Raman studies [11]. Assignment of the 193 cm-1 RBM centered at ~2.86 eV excitation energy is more problematic. As seen in Figure 3.2(b), there are several candidates corresponding to E_{33} or E_{44} excitations of a number of mod 2 semiconducting chiralities (green triangles) from the $2n+m$ = 28 or 31 branches.

Table 3.1 : Observed values for RBM frequency (ω_{RBM}), third optical transition energy (E_{33}), and transition line widths (Γ_{33}) obtained from the Raman data for a given (n, m) chirality nanotube with diameter d_t and chiral angle θ. *Energy is for E_{44} (see discussion).

(n, m)	d_t (nm)	θ (deg)	ω_{RBM} (cm^{-1})	E_{33} (eV)	Γ_{33} (meV)
(13,0)	1.231	0	230	2.72	115
(12,2)	1.027	7.59	228	2.73	123
(11,4)	1.054	14.92	224	2.78	130
(10,6)	1.097	21.79	216	2.81	118
(9,8)	1.154	28.05	204	2.81	115
(11,1)	0.903	4.31	256	2.88	113
(10,3)	0.924	12.73	251	—	—
(9,5)	0.965	20.63	242	—	—
(8,7)	1.018	27.8	230	—	—
(14,3)	1.231	9.52	193	2.86*	111

The closest in frequency are the (15,1), (14,3), and (10,8) chiralities at 195.5 cm^{-1}, 193.3 cm^{-1}, and 194.5 cm^{-1}, respectively. We assign this feature as the (14,3) RBM due to its close match to both the expected frequency and the relative position of its transition energy with respect to that for the $2n+m = 23$ and 26 branches (see also later discussion). Knowledge of which $2n+m$ branches are responsible for the observed features in Fig. 3.2(a) gives direct information on the number of chiralities, and their expected frequencies, that should appear in the RBM spectrum for that branch. This list of possible SWCNT species present in this particular sample was used as an aid to guide the deconvolution of single RBM spectra into their individual

chirality components. Extraction of the individual components allowed construction of the excitation profiles for each observed chirality. Example profiles for four species are shown in Figure 3.3. The experimental excitation profiles were then fit to the resonance Raman line shape function for Stokes scattering [11, 35, 36]:

$$I_{RBM}(n,m) = \frac{M}{[(E_L - E_{ii})^2 + \Gamma_{el}^2/4)][(E_L - E_{ii} - \hbar\omega_{RBM})^2 + \Gamma_{el}^2/4)} \tag{3.1}$$

Here, M incorporates absorption and exciton-phonon coupling matrix elements and sampling conditions, while E_{ii} and E_L are transition and excitation energies, respectively. Fits to eqn. 3.1 were performed with the RBM frequency (ω_{RBM}) fixed to the experimental values and were used to extract the values for the transition energy E_{33} and broadening factor Γ_{33} as adjustable fitting parameters. The results are summarized in Table 3.1.

Finally, I plot in Figure 3.4 the observed RBM frequencies as a function of inverse diameter (d_t) to obtain the coefficients A and B in the usual expression used to relate the two parameters:

$$\omega_{RBM} = \frac{A}{d_t} + B \tag{3.2}$$

A best fit line to the experimental data yields A=219.3 nm cm^{-1} and B=14.7 cm^{-1}, in accord with other values reported in the literature [2,11]. The excellent linear fit provides additional confidence that the chosen (n, m) assignments are correct.

3.2 Photoluminescence Spectra

A 2D PLE intensity map for our sample is shown in Fig. 3.5. The branching patterns observed in the analogous Raman excitation plot are not as well defined for the PLE

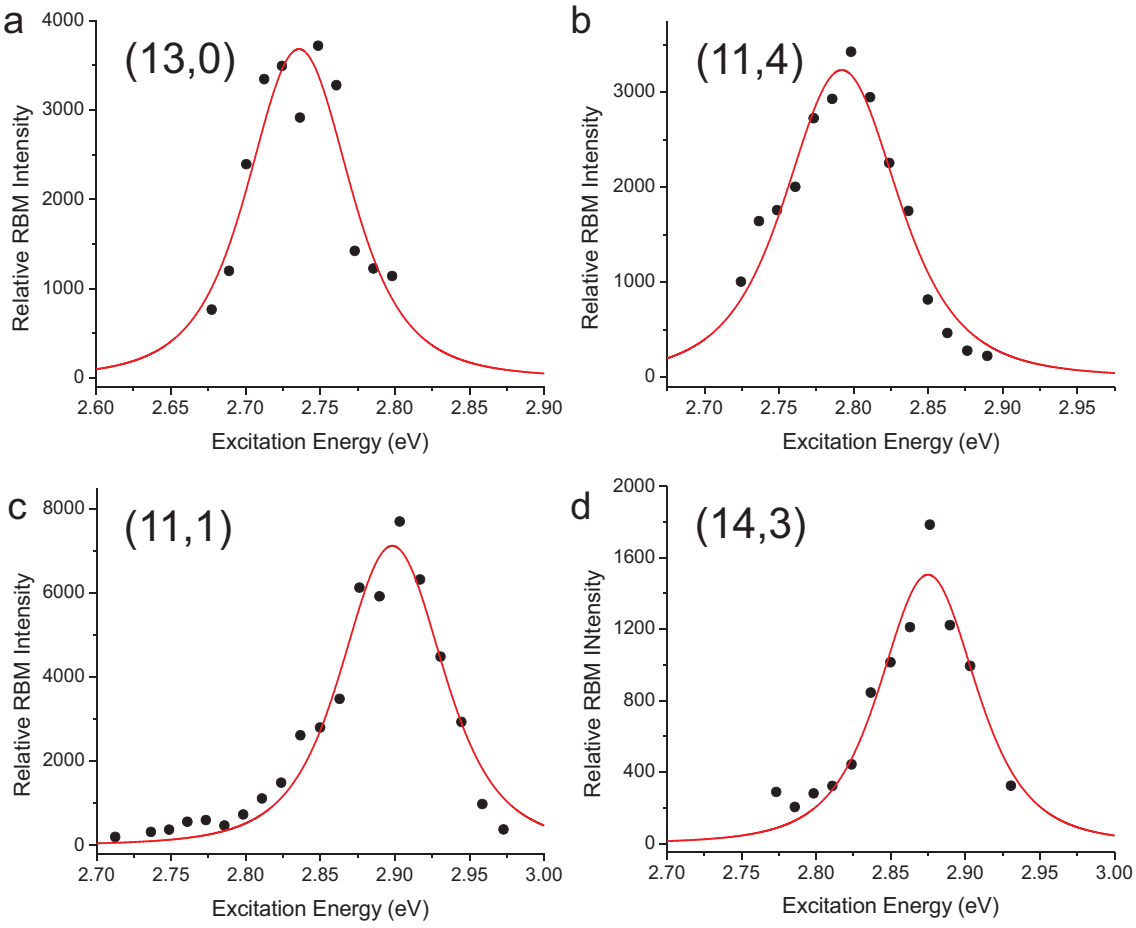

Figure 3.3 : Resonant Raman excitation profiles for four selected nanotube chiralities. Lines are fits according to eqn. 3.1 of the experimental data (dots), from which Γ values are extracted: a) (13,0), Γ =115 meV; b) (11,4), Γ =130 meV; c) (11,1), Γ =113 meV; d) (14,3), Γ =111 meV.

map due to the density of spectral features occurring over most of this energy region. However, I was still able to make definitive assignments for 31 E_{33} and E_{44} spectral features.

PL features were assigned by first identifying their E_{11} emission energy. For each emission energy corresponding to a PL feature, an exhaustive list of possible (n, m) assignments was generated from empirical predictions based on fitted PLE data [12].

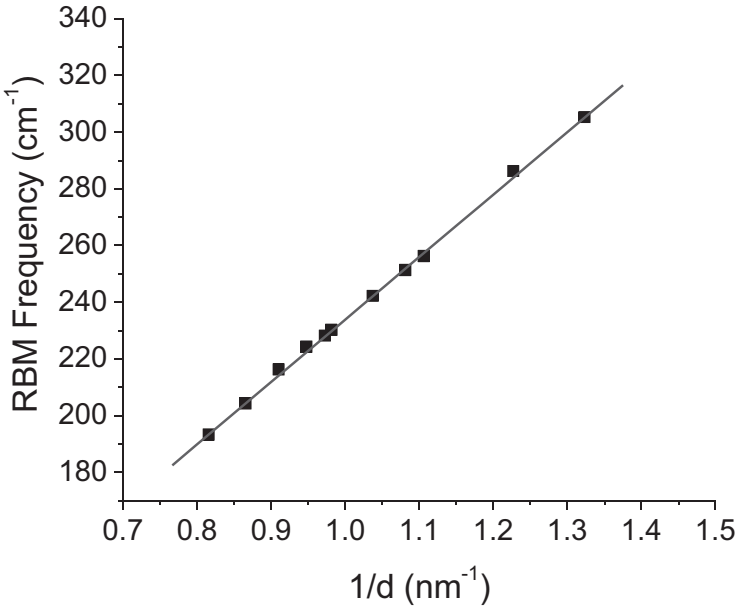

Figure 3.4 : Plot of RBM frequency as a function of inverse nanotube diameter ($1/d_t$). The line is a linear fit to the experimental data points (squares), yielding the parameters A=219.3 nm cm^{-1} and B=14.7 cm^{-1} from eqn. 3.2.

Certain chiralities [such as the (6,5), (8,6), (8,7), (9,7), and others] have E_{11} emission energies that are well-isolated from other chiralities such that only one (n, m) is possible, allowing both the E_{33} and E_{44} excitation energies to be unambiguously assigned for them. In the case where the emission energy was not sufficiently isolated as to result in only one (n, m), the list of possible (n, m) assignments was compared to the known (n, m) chiralities present in this particular sample, as determined by PLE spectroscopy via E_{22} excitation [7]. This list of known chiralities was used to constrain the possible assignments for the higher order PL features. For instances where a single (n, m) assignment was still indeterminable and where the potential assignments displayed a difference in mod characteristic (*i.e.*, one assignment is mod 1, whereas the other is mod 2), an examination of the energy difference between the

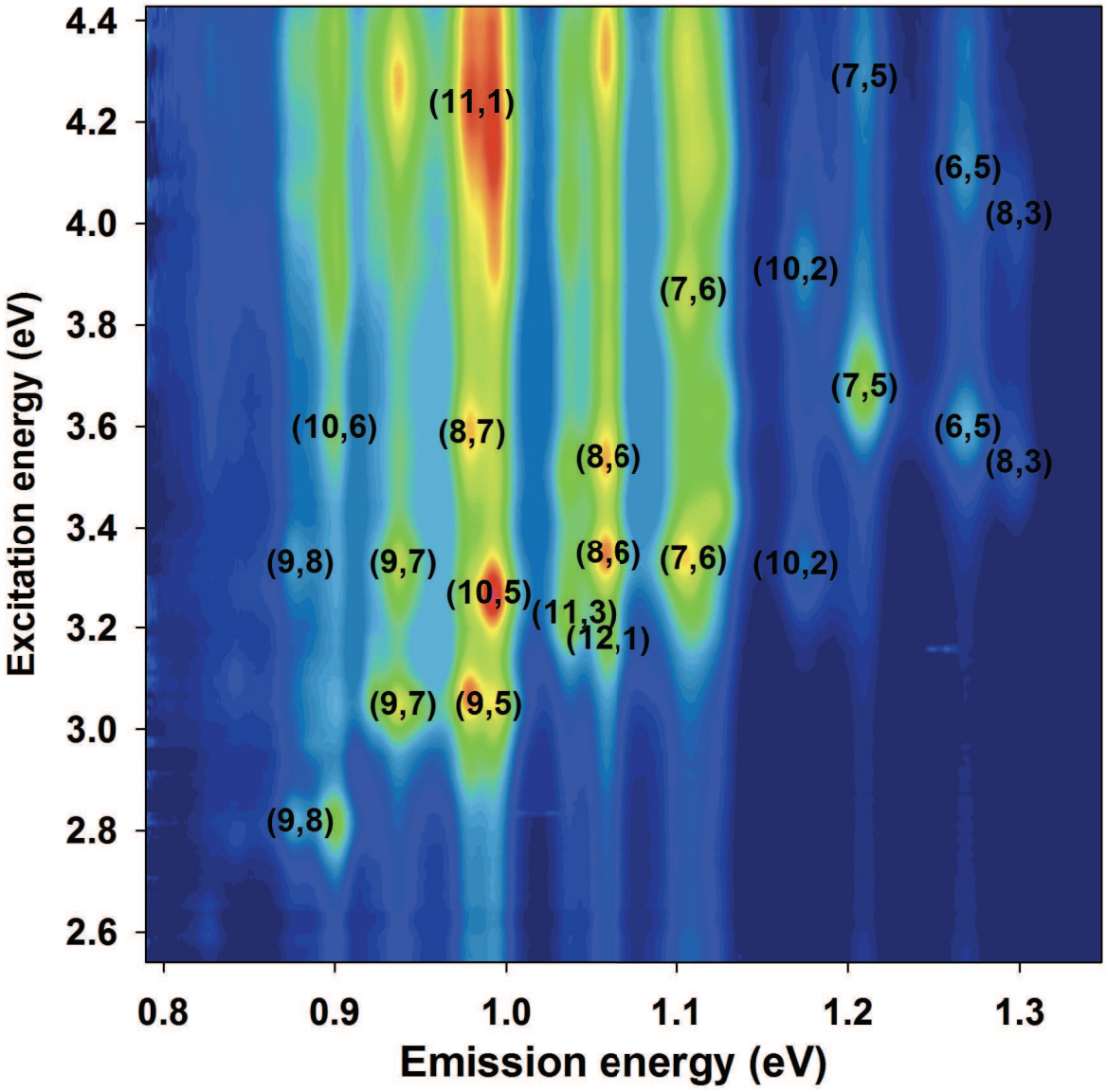

Figure 3.5 : 2D intensity map showing nanotube photoluminescence intensity as a function of emission energy, as excitation energy is varied. Chirality assignments for selected E_{33} and E_{44} features are labeled.

E_{33} and E_{44} features, ΔE, was made. Nanotubes displaying E_{33} /E_{44} features that are relatively closely spaced in energy (ΔE <300 meV) were considered to be more likely of the mod 2 variety, while nanotubes with fairly large ΔE were considered more likely to be mod 1. I also looked at any closely spaced E_{33}/E_{44} features for possible phonon-assisted photoluminescence due to either RBM or G-mode phonons as a possible alternative origin of observed features. Such phonon-assisted PL features were not included in the reported data to simplify the energy analysis.

Additionally, I was able to use the Raman assignments obtained in the 3.2 to anchor certain parts of the PLE map, further enabling assignments of additional chiralities [such as the (10,6) and (9,8) and nearby chiralities]. Finally, to confirm these assignments as well as to suggest assignments for undetermined features, patterns observed in an analogous plot of correlated ETB energies, although offset from the experimental data in a manner similar to that found in the Raman data, provided a useful guide for the assignment of the final transitions not obtained by the above approaches. The resulting assignments and E_{33} and E_{44} transition energies are labeled in Fig. 3.5 and listed in Table 3.2. The listed features (and energies used in the analysis discussed in Chapter 4) are only for those chiralities that have been assigned with the highest confidence.

Table 3.2 : Observed values for third (E_{33}) and fourth (E_{44}) optical transition energies obtained from the PLE data for a given (n, m) chirality nanotube with diameter d_t, and chiral angle θ. *Energies for E_{33} and E_{44} for these chiralities must be exchanged. Because of the cross-over effect (see Chapter 4) energy ordering is reversed in these cases.

(n, m)	d_t (nm)	θ (deg)	E_{33} (eV)	E_{44} (eV)
(6,4)*	0.692	23.41	3.93*	—
(6,5)	0.757	27	3.6	4.11
(8,3)*	0.782	15.3	3.53*	4.02*
(7,5)	0.829	24.5	3.68	4.29
(7,6)	0.895	27.46	3.34	3.87
(10,2)*	0.884	8.95	3.33*	3.91*
(9,4)*	0.916	17.48	3.43*	3.62*
(8,6)	0.966	25.28	3.35	3.54
(11,1)	0.916	4.31	—	4.24
(9,5)	0.976	20.63	3.05	—
(8,7)	1.032	27.8	3.07	3.59
(12,1)*	0.995	3.96	3.18*	—
(11,3)*	1.014	11.74	3.23*	3.51*
(10,5)	1.05	19.11	3.27	—
(9,7)	1.103	25.87	3.05	3.33
(10,6)	1.111	21.79	2.82	3.6
(9,8)	1.17	28.05	2.82	3.33
(10,8)	1.24	26.33	2.79	3.1

Chapter 4

Discussion

4.1 Transition Level and Raman Intensities

It is important to note that the intensities observed in the RBM spectra obtained here are about an order of magnitude weaker than found for spectra obtained at resonance with the E_{22} transitions. This behavior is also reported in ref. [2], in which RBM features resonant with E_{33} or E_{44} transitions are significantly weaker than those resonant with E_{11} or E_{22}. These reduced intensities for the higher lying nanotube transitions continue the trend previously observed in ref. [37]. In that work, RBM intensities observed at resonance with E_{22} excitation were significantly lower (by one or more orders of magnitude) than those observed at resonance with E_{11} excitation for identical nanotube chiralities. Decreased intensities were attributed to more rapid dephasing of the E_{22} exciton, as manifested by an increase in gamma values [37]. Resonance line widths were found to increase from 20-30 meV in E_{11} to 50-70 meV for E_{22}. We find here (Table 3.1) that gamma values continue to increase on going to E_{33} excitation, with observed values being twice those found for E_{22}, and ranging from 110 to 130 meV. These results suggest that exciton decay rates will further increase as one excites to higher energy, as is consistent with the stronger vibronic interactions and accelerated relaxation processes found at higher excitation energies in molecular photophysics.

An additional contributing factor to intensity behavior within the E_{33} and E_{44}

transitions is how the exciton-phonon coupling is affected at these excitation levels. For example, it has been observed that the chiral angle dependence of exciton-phonon coupling results in a decrease in RBM intensity as chiral angle θ increases within a particular $2n+m$ branch [10,38,39]. Such a trend is in fact observed for the $2n+m$=26 branch with E_{33} excitation. Progressing from the zigzag (13,0) (θ= 0$\circ$) to near-armchair (9,8) (θ= 28$\circ$) chiralities, we observe a steady decrease in intensity of the respective RBM. Another anticipated effect on the exciton-phonon coupling is its dependence on the semiconductor type. Previous reports [8, 38, 40, 41] have shown that with E_{22} excitation, mod 2 tubes have larger coupling (and therefore RBM intensity) than mod 1. In general, this dependence is reversed in E_{11} excitation, and is also expected to reverse again for the E_{33} transition. Thus, for excitation into E_{33}, we should expect to see primarily mod 1 RBM features. This is in agreement with the chiralities observed in our Raman spectra. Except for the (14,3) chirality, all observed semiconductors are mod 1. That the mod 2 (14,3) chirality is observed suggests that resonant excitation is with E_{44} rather than E_{33} for this nanotube. This hypothesis is confirmed in the next section.

4.2 Transition Crossing and Observed Energies

E_{33} transition energies determined from the Raman and PLE results are on average 70 meV larger than those calculated in the ETB approach. This positive deviation is in good alignment with the previous results of Araujo *et al.* [2]. The trends found in the E_{44} energies are more complex. The positive deviations in observed energies can be understood in terms of how the exciton many-body contributions change as one accesses the higher-order nanotube transitions. The behavior of these many-body effects can be extracted from the experimental transition energies by using an analysis

similar to that used in ref. [2]. I find that applying this analysis to the data reveals interesting new behavior that is not evident in the previous analysis as applied to larger diameter nanotubes.

The nanotube transition energy can be dissected into contributions from the diameter-dependent single-particle energy expected from quantum confinement of the 2D electronic structure of graphene, the chiral-angle (θ) dependent effects of trigonal warping, and many-body excitonic effects. The quantum confinement energy may be given as $h\nu_F(4p/3d_t)$, where ν_F is the Fermi velocity, d_t is the nanotube diameter, and p=1,2,3,4,5 for E_{11}^S, E_{22}^S, E_{11}^M, E_{33}^S, and E_{44}^S, respectively [42]. Trigonal warping perturbation [30, 31] raises or lowers these energies in a chiral angle-dependent fashion to produce the now-familiar branching patterns observed in PLE and Raman data [2, 7, 9–11]. This contribution may be approximated by the term $\beta_p \cos 3\theta/d_t^2$, where β_p is +0.42 for E_{33} (-0.40 for E_{44}) for mod 2 nanotubes, and is 0.42 for E_{33} (+0.40 for E_{44}) for mod 1 nanotubes [2]. What remains after removal of this term and the linearly dependent quantum confinement term from the experimentally determined transition energies is the excitonic contribution of the many-body effects, which may be approximated by a logarithmic scaling of energies [1,17], also dependent on p/d_t. Each of these contributions is expressed in Eqn. 4.1 [2],

$$E_{ii}(p, d_t) - \beta_p \cos 3\theta/d_t^2 = a\frac{p}{d_t}\left(1 + b\log\frac{c}{p/d_t}\right) \tag{4.1}$$

in which a, b, and c are fitting parameters, and $E_{ii}(p, d_t)$ is the experimentally determined transition energy.

In Figure 4.1(a), the trigonal warping term is subtracted from the experimentally determined E_{33}^S and E_{44}^S transition energies and plot the result as a function of p/d_t. These results are compared to two different trend lines. The first (lower line) is the

result of eqn. 4.1 when applied to E_{11}^S and E_{22}^S transition energies, with a, b, and c equaling 1.049 eV nm, 0.456, and 0.812 nm^{-1}, respectively [2]. The work of Araujo *et al.* showed that the E_{33}^S and E_{44}^S energies deviate from this behavior by the term $0.305/d_t$. I show that resulting E_{33}^S and E_{44}^S trend line as the second, upper curve. Inspection of Fig. 4.1(a) leads to two notable observations. The first is that, while the majority of the observed chiralities appear to fall on a smooth trend line, a handful of designated chiralities (highlighted by circles) add significant scatter to this pattern. The second observation is that although energies for the largest diameter nanotubes in our data set (0.9 to 1.2 nm) reproduce with excellent agreement the E_{33}^S and E_{44}^S trend line of ref. [2], energies for the smallest diameter nanotubes show significant negative deviation from this trend (beginning at d_t values of about 0.9 nm). This deviation is most dramatically shown by the E_{44} value for the (6,5) chirality, which is so low that it reaches the original E_{11} and E_{22} scaling law trend line. The problem of the appearance of significant scatter for certain chiralities is addressed first. The negative deviation of the E_{33} and E_{44} scaling behavior for small-diameter nanotubes is discussed in the section 4.3.

The large deviation and scatter from the E_{33} and E_{44} scaling law line for the (6,4), (8,3), (9,4), (10,2), (11,3), and (12,1) chiralities is a previously unobserved manifestation of a trigonal warping effect that only becomes evident as one accesses the higher lying transitions of small-diameter nanotubes. This behavior is, in a sense, a more extreme consequence of the underlying causes of the branching energy spread found along a given $2n+m$ value. Within the graphene Brillouin zone, trigonal warping results in equienergy contours that are distorted from circles into a more triangular shape, with an apex along the K-M line and base along the Γ-K line. For mod 2 semiconducting types, the E_{11} and E_{33} transitions originate in the K-M valley, while E_{22}

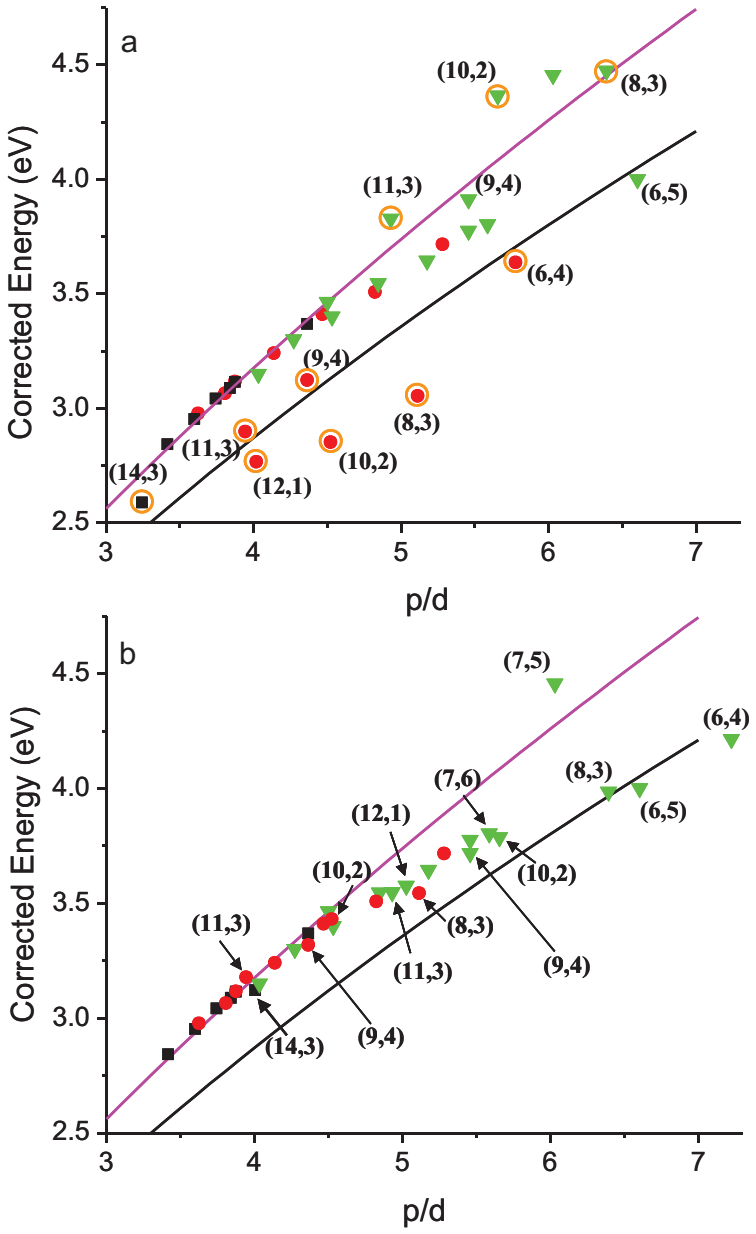

Figure 4.1 : Corrected E_{33} and E_{44} transition energies (E_{expt} - $\beta_p \cos 3\theta/d_t^2$) as a function of p/d_t, where p=4 and 5, respectively. E_{33} data are obtained from Raman (black squares) and PLE (red circles) measurements, while E_{44} data (green triangles) are obtained from the PLE measurement. Energy assignments to E_{33} and E_{44} features are chosen directly from their respective ordering from the experimental results. Results are compared to scaling law lines from ref. [2] for E_{33} and E_{44} (upper line) and E_{11} and E_{22} (lower line behavior), see eqn. 4.1. Chiralities showing significant scatter from the scaling law behavior are designated and highlighted by circles. b) The data of part (a) replotted after correcting the energy ordering of the (14,3), (12,1), (11,3), (10,2), (9,4), (8,3), and (6,4) chiralities for the effect of branch cross-over.

and E_{44} originate from the Γ-K valley. As a result, as one goes from near-armchair to near-zigzag chiralities within a $2n+m$ branch, the E_{11} and E_{22} energies curve toward each other, as do the E_{33} and E_{44} energies. These higher-order transitions occur in a region of greater trigonal distortion of the energy surfaces so that the difference between E_{33} and E_{44} energies can become quite small. In particular cases, the effect can even reverse the ordering of their energies. This reversal of energy ordering can be seen in a Kataura plot of ETB calculated energies vs. RBM frequency (Figure 4.2). In this plot, the E_{33} and E_{44} energies are predicted to cross over for certain chiralities at these higher energies. Note that the smallest diameter branches are most strongly affected by this phenomenon. Of the chiralities observed, the (6,4), (8,3), (9,4), (10,2), (11,3), and (12,1) nanotubes (highlighted in Fig. 4.2) would be expected to show this cross-over effect. One can conclude that the E_{33}/E_{44} cross-over phenomenon is responsible for the scattered behavior of these chiralities seen in Fig. 4.1(a).

The results shown in Fig. 4.2 suggest that for these higher order transitions, the correct E_{ii} assignment is not necessarily obtained by simple ordering of spectral features according to transition energy. Specifically, for the (6,4), (8,3), (9,4), (10,2), (11,3), and (12,1) nanotubes, an exchange of the E_{33} and E_{44} energy assignments shown in Table 3.2 is indicated. To appropriately account for this assignment change in the analysis of Fig. 4.1(a), the correct values of β_p and p (determined by choice of E_{ii}) must be paired with the corresponding energies. The results after applying this energy reordering are plotted in Fig. 4.1(b). A smooth behavior across the whole range of data is now seen. This analysis can therefore be taken as strong experimental evidence supporting the energy cross-over effect. Thus, at higher energies care must be taken in assigning E_{ii} values to observed spectral features. E_{ii} should not be

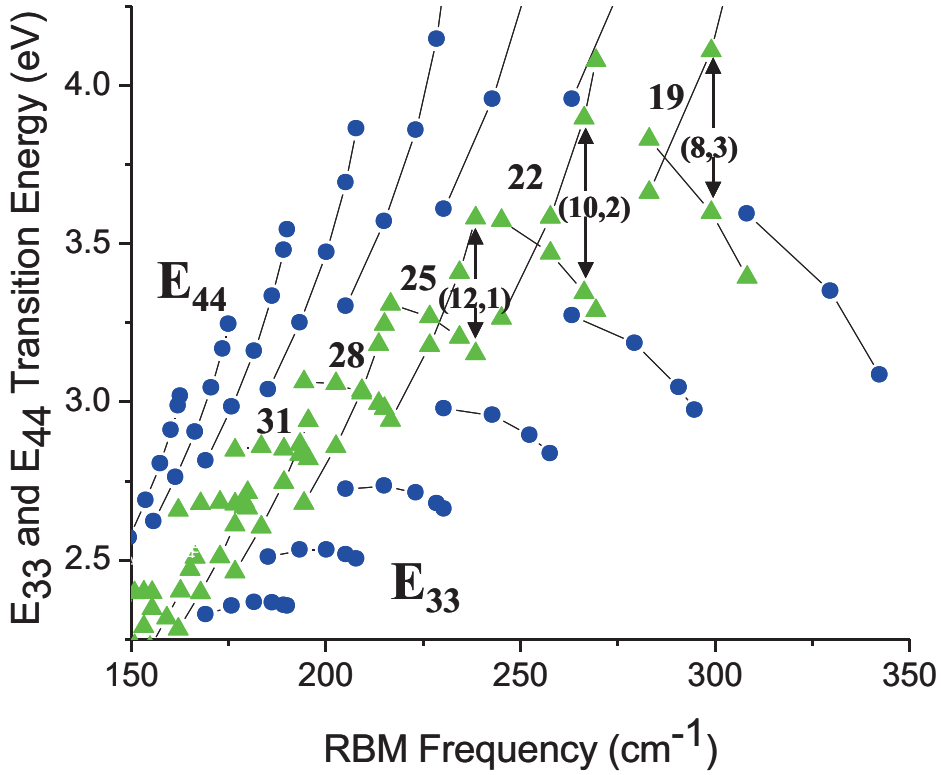

Figure 4.2 : ETB-calculated [3] E_{33} and E_{44} transition energies as a function of RBM frequency for mod 1 (circles) and mod 2 (triangles) species. Branch cross-over effect of E_{33} and E_{44} energy behaviors is illustrated, with specific chiralities and branches relevant to Fig. 4.1(a) highlighted.

deduced simply on the basis of energy ordering, but more correctly from its basis in symmetry with respect to the K-point as defined by the ordering of the respective cutting lines.

One consequence of the minimization of the energy difference between E_{33} and E_{44} and the crossing over of these transitions in mod 2 nanotubes is the possibility of observing Raman interference effects [43, 44]. While Raman interference could potentially impact the observed excitation profile for the (14,3) chirality, the symmetric

appearance of the data [Fig. 3.3(d)] suggests that any interference effects are minimized. This is likely a result of the E_{33} transition strength being significantly reduced via exciton-phonon coupling effects [37–41]. For the remaining chiralities observed in the Raman spectra, interference effects are not likely since these are mod 1 nanotubes whose E_{33} and E_{44} energies spread away from each other (see Fig. 4.2).

Deviations from the trends found within the scaling law analysis can thus be used to identify the energy cross-over effect, and may be used as an additional tool to aid in assigning spectral features. This new tool can be applied to make a secure assignment of the (14,3) feature observed in the RBM Raman excitation profiles. As seen in Fig. 4.1(a), if this feature is identified as the E_{33} transition, a significant deviation from the scaling-law line results, in a region where excellent agreement is found for similar diameter nanotubes. Figure 4.1(b) shows that cross-over of the E_{33} and E_{44} transitions is expected to occur for this chirality. If the (14,3) spectral feature is instead assigned to the E_{44} transition, close agreement to the scaling-law trend (see Fig. 6b) is observed. Assignment as the E_{44} feature also preserves the trend in expected intensities for mod 2 semiconductor types, as discussed in the previous section. Finally, note that the (7,5) feature assigned as E_{44} also deviates significantly from the expected trends inFig. 4.1(b). It is likely that this feature is instead an E_{55} transition. This revised assignment will also bring the (7,5) point into alignment with the generally observed trends.

4.3 Curvature Effects on Higher Order Exciton Energies

The two different trend lines in Fig. 4.1 effectively illustrate the difference in behavior of SWCNT excitonic energy contributions in higher energy transitions. The many-body effects contribute as the difference $(\Sigma - E_{bind})$ between the electron self-energy,

Σ, and the exciton binding energy, E_{bind}. This difference is found to be significantly larger for E_{33} and E_{44} because the self-energy increases considerably relative to E_{bind} for higher order transitions [45], and is suggested to be the origin of the differing trend lines in Fig. 4.1. Additionally, at smaller diameters, Sato *et al.* [45] found a significant chiral angle dependence and/or energy spread in the E_{33} and E_{44} many-body contributions that is not present for E_{11} and E_{22}. The energy spread in the many-body term appears to arise primarily from E_{bind}. Thus, while the chiral angle dependence in E_{11} and E_{22} appears mainly as the branching energy spread in the single particle energies, the energy spread in the many-body term adds a significant source of chiral angle dependence in E_{33} and E_{44}.

It is important to note, however, that the single-particle and many-body sources of energy spread contribute in opposite directions [45]. In the case of mod 2 semiconductors, for example, the single-particle contribution is positive, while that from the many-body chiral-angle dependence is negative. Thus, when we apply the $\beta_p \cos 3\theta / d_t^2$ term to remove the single-particle energy spread, the negative-going component from the many-body effects remains. The net effect is that applying the $\beta_p \cos 3\theta / d_t^2$ term overcorrects for energy spread behavior in small-diameter nanotubes and results in the negative-going trend away from the E_{33} and E_{44} scaling law line shown in Fig. 4.1. That this is predicted to be most pronounced for near-zigzag chiralities [45] is supported by the data. In contrast, one would expect the opposite behavior for mod 1 semiconductors, with an overcorrection resulting in positive deviations from the scaling law line for these nanotube types. However, the mod 1 nanotubes observed in these results are near-armchair chiralities, for which the energy spread effect should be minimal. The negative-going trend in these types arises from another effect.

In general, the electron self-energy is expected to be only weakly dependent on

chiral angle [45]. For higher-order transitions and smaller diameters, however, this expectation breaks down and a significant θ-dependence is predicted [45]. In particular, in E_{44}, Σ for mod 1 nanotubes is expected to decrease significantly as chiral angle increases. Near-armchair mod 1 chiralities should therefore show a significant negative-going trend in the plots of Figs. 4.1(a) and 4.1(b). This is in fact what is observed, with the effect most clearly being seen for the (6,5) and (7,6) chiralities. The decrease in Σ as θ increases is predicted to become less important in E_{33} and for mod 2 nanotubes, but it can be an additional minor source of the negative-going trend observed in the data.

4.4 Extension of Work Presented Here

In light of the experimental results presented here and their respective physical meaning in the context of carbon nanotube electronic structure, it is useful to quickly examine a related work by another researcher group and examine how this work impacts theirs.

Although considered to be one of the more widely employed methods for calculating electronic transition energies in SWCNTs, the tight-binding method does not often calculate accurately experimentally determined optical transition energies easily although it does reproduce the overall relative energy patterns and branch structure in the family of carbon nanotube species well. Other calculation methods that are considered more accurate, such as density functional theory, are generally more computationally costly and do not result in useful analytical expressions for calculating transition energies of any SWCNT species with only a few input parameters. Barone *et al.* developed a hybrid functional method that can calculate accurately and with little computational cost optical transition energies of both metallic and semiconduct-

ing SWCNTs, including higher order optical transitions [5, 46]. Unfortunately, the quantum chemistry and carbon nanotube communities did not readily accept this new method because it was thought the method could not account for excitonic effects.

Table 4.1 : Comparison of experimental E_{33}^S values* [4] with those calculated by hybrid functional theory† [5] and ETB method‡ [6].

(n,m)	Expt (eV)*	HFT (eV)†	ETB (eV)‡	ΔE (Expt-HFT)	ΔE (expt-ETB)
(6,4)	3.93	3.96	-	-0.03	-
(6,5)	3.6	3.68	4.073	-0.08	-0.473
(8,6)	3.35	3.4	3.634	-0.05	-0.284
(10,5)	3.27	3.33	3.550	-0.06	-0.280
(10,6)	2.82	2.82	3.071	0	-0.251
(10,8)	2.79	2.78	2.975	0.01	-0.185
(13,0)	2.72	2.75	3.051	-0.03	-0.331

As shown in Tables 4.1 and 4.2, the hybrid functional calculation reproduces with much higher accuracy the experimentally observed E_{33}^S and E_{44}^S transition energies than one of the most sophisticated ETB calculations [6] currently available with deviations on the order of tens of meV for the hybrid functional theory and hundreds of meV for ETB. As a result, these experimental transition energies justify the hybrid functional technique for accurately capturing real physical phenomena such as exchange and exception effects in the calculation of SWCNT optical transition energies.

Table 4.2 : Comparison of experimental E_{44}^S values* [4] with those calculated by hybrid functional theory† [5] and ETB method‡ [6].

(n, m)	Expt (eV)*	HFT (eV)†	ETB (eV)‡	ΔE (Expt-HFT)	ΔE (expt-ETB
(6,4)	-	4.21	-	-	-
(6,5)	4.11	4.32	4.869	-0.21	-0.759
(8,6)	3.54	3.63	4.022	-0.09	-0.482
(10,5)	-	4.27	3.707	-	-
(10,6)	3.6	3.68	3.990	-0.08	-0.390
(10,8)	3.1	3.14	3.428	-0.04	-0.328
(13,0)	-	3.85	4.519	-	-

Chapter 5

Conclusion

Extending Raman and photoluminescence excitation profiling of nanotubes into the UV has provided access to higher lying exciton transitions for small-diameter nanotubes. This extended excitation range has demonstrated a further continuation of some previously observed trends, including exciton-phonon coupling trends, the increase in magnitude of Γ, and scaling law behavior of the largest diameter nanotubes in our study. More importantly, however, this has also allowed the observation of new effects. I have experimentally verified an extension of trigonal warping effects by showing that energy cross-over behavior along selected $2n+m$ branch lines has physically observable consequences. Additionally, a number of predictions of recent theoretical studies [45] on the chirality dependence of many-body effects have now been experimentally verified. The observation of a negative deviation from the large diameter E_{33} and E_{44} scaling law trend line of Araujo *et al.* [2] clearly demonstrates the existence of these effects, and also confirms the sign of chirality-dependent trends expected for both self-energy and binding energy. These results provide an experimental foundation for further probing the potential sensitivity of these spectral effects to nanotube environment. Recognizing and understanding the trends observed here can greatly assist in the assignment of spectral features in this increasingly crowded spectral region as the E_{ii} transitions tend to broaden and merge together. The scaling law analysis employed here can be a particularly powerful tool in that regard. This region will be a fruitful arena in which to further explore nanotube properties that

become evident only at small diameters and high energies.

Bibliography

[1] A. Jorio, C. Fantini, M. A. Pimenta, R. B. Capaz, G. G. Samsonidze, G. Dresselhaus, M. S. Dresselhaus, J. Jiang, N. Kobayashi, A. Grüneis, and R. Saito, "Resonance Raman Spectroscopy (n,m)-Dependent Effects in Small-Diameter Single-Wall Carbon Nanotubes," Phys. Rev. B **71**, 075401 (2005).

[2] P. T. Araujo, S. K. Doorn, S. Kilina, S. Tretiak, E. Einarsson, S. Maruyama, H. Chacham, M. A. Pimenta, and A. Jorio, "Third and Fourth Order Optical Transitions in Semiconducting Carbon Nanotubes," Phys. Rev. Lett. **98**, 067401 (2007).

[3] G. G. Samsonidze, R. Saito, N. Kobayashi, A. Grüneis, J. Jiang, S. G. Chou, G. Dresselhaus, and M. S. Dresselhaus, "Family Behavior of the Optical Transition Energies in Single-Wall Carbon Nanotubes of Smaller Diameters," Appl. Phys. Lett. **85**, 5703 (2004).

[4] E. H. Haroz, S. M. Bachilo, R. B. Weisman, and S. K. Doorn, "Curvature Effects on the E_{33} and E_{44} Exciton Transitions in Semiconducting Single-Walled Carbon Nanotubes," Phys. Rev. B **77**, 125405 (2008).

[5] V. Barone, J. E. Peralta, M. Wert, J. Heyd, and G. E. Scuseria, "Density Functional Theory Study of Optical Transitions in Semiconducting Single-Wall Carbon Nanotubes," Nano Lett. **5**, 1621 (2005).

[6] A. R. T. Nugraha, R. Saito, K. Sato, P. T. Araujo, A. Jorio, and M. S. Dres-

selhaus, "Dielectric Constant Model for Environmental Effects on the Exciton Energies of Single Wall Carbon Nanotubes," Appl. Phys. Lett. **97**, 091905 (2010).

[7] S. M. Bachilo, M. S. Strano, C. Kittrell, R. H. Hauge, R. E. Smalley, and R. B. Weisman, "Structure-Assigned Optical Spectra of Single-Walled Carbon Nanotubes," Science **298**, 2361 (2002).

[8] S. K. Doorn, D. A. Heller, P. W. Barone, M. L. Usrey, and M. S. Strano, "Resonant Raman Excitation Profiles of Individually Dispersed Single Walled Carbon Nanotubes in Solution," Appl. Phys. A **78**, 1147 (2004).

[9] C. Fantini, A. Jorio, M. Souza, M. S. Strano, M. S. Dresselhaus, and M. A. Pimenta, "Optical Transition Energies for Carbon Nanotubes from Resonant Raman Spectroscopy: Environment and Temperature Effects," Phys. Rev. Lett. **93**, 147406 (2004).

[10] H. Telg, J. Maultzsch, S. Reich, F. Hennrich, and C. Thomsen, "Chirality Distribution and Transition Energies of Carbon Nanotubes," Phys. Rev. Lett. **93**, 177401 (2004).

[11] J. Maultzsch, H. Telg, S. Reich, and C. Thomsen, "Radial Breathing Mode of Single-Walled Carbon Nanotubes: Optical Transition Energies and Chiral-Index Assignment," Phys. Rev. B **72**, 205438 (2005).

[12] R. B. Weisman and S. M. Bachilo, "Dependence of Optical Transition Energies on Structure for Single-Walled Carbon Nanotubes in Aqueous Suspension: An Empirical Kataura Plot," Nano Lett. **3**, 1235 (2003).

[13] M. S. Strano, S. K. Doorn, E. H. Haroz, C. K. Kittrell, R. H. Hauge, and R. E.

Smalley, "Assignment of (n, m) Raman and Optical Features of Metallic Single-Walled Carbon Nanotubes," Nano Lett. **3**, 1091 (2003).

[14] H. Kataura, Y. Kumazawa, Y. Maniwa, I. Umezu, S. Suzuki, Y. Ohtsuka, and Y. Achiba, "Optical Properties of Single-Wall Carbon Nanotubes," Synthetic Metals **103**, 2555 (1999).

[15] M. S. Strano, "Probing Chiral Selective Reactions Using a Revised Kataura Plot for the Interpretation of Single-Walled Carbon Nanotube Spectroscopy," J. Am. Chem. Soc. **125**, 16148 (2003).

[16] T. Ando, "Excitons in Carbon Nanotubes," J. Phys. Soc. Jpn. **66**, 1066 (1997).

[17] C. L. Kane and E. J. Mele, "Electron Interactions and Scaling Relations for Optical Excitations in Carbon Nanotubes," Phys. Rev. Lett. **93**, 197402 (2004).

[18] H. Zhao and S. Mazumdar, "Electron-Electron Interaction Effects on the Optical Excitations of Semiconducting Single-Walled Carbon Nanotubes," Phys. Rev. Lett. **93**, 157402 (2004).

[19] C. D. Spataru, S. Ismail-Beigi, L. X. Benedict, and S. G. Louie, "Excitonic Effects and Optical Spectra of Single-Walled Carbon Nanotubes," Phys. Rev. Lett. **92**, 077402 (2004).

[20] V. Perebeinos, J. Tersoff, and P. Avouris, "Scaling of Excitons in Carbon Nanotubes," Phys. Rev. Lett. **92**, 257402 (2004).

[21] R. B. Capaz, C. D. Spataru, S. Ismail-Beigi, and S. G. Louie, "Diameter and Chirality Dependence of Exciton Properties in Carbon Nanotubes," Phys. Rev. B **74**, 121401(R) (2006).

[22] J. Jiang, R. Saito, G. G. Samsonidze, A. Jorio, S. G. Chou, G. Dresselhaus, and M. S. Dresselhaus, "Chirality Dependence of Exciton Effects in Single-Wall Carbon Nanotubes: Tight-Binding Model," Phys. Rev. B **75**, 035407 (2007).

[23] A. Jorio, R. Saito, J. H. Hafner, C. M. Lieber, M. Hunter, T. McClure, G. Dresselhaus, and M. S. Dresselhaus, "Structural (n,m) Determination of Isolated Single-Wall Carbon Nanotubes by Resonant Raman Scattering," Phys. Rev. Lett. **86**, 1118 (2001).

[24] S. K. Doorn, L. Zheng, M. J. O'Connell, Y. Zhu, S. Huang, and J. Liu, "Raman Spectroscopy and Imaging of Ultralong Carbon Nanotubes," J. Phys. Chem. B **109**, 3751 (2005).

[25] S. Arepalli, "Laser Ablation Process for Single-Walled Carbon Nanotube Production," J. Nanosci. Nanotech. **4**, 317 (2004).

[26] S. Lebedkin, F. Hennrich, T. Skipa, and M. M. Kappes, "Near-Infrared Photoluminescence of Single-Walled Carbon Nanotubes Prepared by the Laser Vaporization Method," J. Phys. Chem. B **107**, 1949 (2003).

[27] Y. Murakami, E. Einarsson, T. Edamura, and S. Maruyama, "Polarization Dependent Optical Absorption Properties of Single-Walled Carbon Nanotubes and Methodology for the Evaluation of their Morphology," Carbon **43**, 2664 (2005).

[28] K. Hata, D. N. Futaba, K. Mizuno, T. Namai, M. Yumura, and S. Iijima, "Water-Assisted Highly Efficient Synthesis of Impurity-Free Single-Walled Carbon Nanotubes," Science **306**, 1362 (2004).

[29] T. Michel, M. Paillet, J. C. Meyer, V. N. Popov, L. Henrard, and J. L. Sauvajol, "E_{33} and E_{44} Optical Transitions in Semiconducting Single-Walled Carbon

Nanotubes: Electron Diffraction and Raman Experiments," Phys. Rev. B **75**, 155432 (2007).

[30] R. Saito, G. Dresselhaus, and M. S. Dresselhaus, "Trigonal Warping Effect of Carbon Nanotubes," Phys. Rev. B **61**, 2981 (2000).

[31] S. Reich and C. Thomsen, "Chirality Dependence of the Density-of-States Singularities in Carbon Nanotubes," Phys. Rev. B **62**, 4273 (2000).

[32] J. Kürti, V. Zólyomi, M. Kertesz, and G. Sun, "The Geometry and the Radial Breathing Mode of Carbon Nanotubes: Beyond the Ideal Behaviour," New J. Phys. **5**, 125 (2003).

[33] M. J. O'Connell, S. M. Bachilo, C. B. Huffman, V. C. Moore, M. S. Strano, E. H. Haroz, K. L. Rialon, P. J. Boul, W. H. Noon, C. Kittrell, J. Ma, R. H. Hauge, R. B. Weisman, and R. E. Smalley, "Band Gap Fluorescence from Individual Single-Walled Carbon Nanotubes," Science **297**, 593 (2002).

[34] V. N. Popov, "Curvature Effects on the Structural, Electronic and Optical Properties of Isolated Single-Walled Carbon Nanotubes within a Symmetry-Adapted Non-Orthogonal Tight-Binding Model," New J. Phys. **6**, 17 (2004).

[35] M. A. Pimenta, A. Marucci, S. A. Empedocles, M. G. Bawendi, E. B. Hanlon, A. M. Rao, P. C. Eklund, R. E. Smalley, G. Dresselhaus, and M. S. Dresselhaus, "Raman Modes of Metallic Carbon Nanotubes," Phys. Rev. B **58**, R16016 (1998).

[36] R. M. Martin and L. M. Falicov, "Resonant Raman Scattering," in *Light Scattering in Solids*, edited by M. Cardona and G. Güntherodt (Springer-Verlag, Berlin, 1975), vol. 8, p. 79.

[37] B. C. Satishkumar, S. V. Goupalov, E. H. Hároz, and S. K. Doorn, "Transition Level Dependence of Raman Intensities in Carbon Nanotubes: The Role of Exciton Decay," Phys. Rev. B **74**, 155409 (2006).

[38] S. V. Goupalov, B. C. Satishkumar, and S. K. Doorn, "Excitation and Chirality Dependence of the Exciton-Phonon Coupling in Carbon Nanotubes," Phys. Rev. B **73**, 115401 (2006).

[39] M. Machón, S. Reich, H. Telg, J. Maultzsch, P. Ordejón, and C. Thomsen, "Strength of Radial Breathing Mode in Single-Walled Carbon Nanotubes," Phys. Rev. B **71**, 035416 (2005).

[40] S. V. Goupalov, "Chirality Dependence of the Raman Cross Section of Carbon Nanotubes," Phys. Rev. B **71**, 153404 (2005).

[41] S. V. Goupalov, "Optical Transitions in Carbon Nanotubes," Phys. Rev. B **72**, 195403 (2005).

[42] R. Saito, G. Dresselhaus, and M. S. Dresselhaus, *Physical Properties of Carbon Nanotubes* (Imperial College Press, London, 1998).

[43] G. Bussi, J. Menendez, J. Ren, M. Canonico, and E. Molinari, "Quantum Interferences in the Raman Cross Section for the Radial Breathing Mode in Metallic Carbon Nanotubes," Phys. Rev. B, Rapid Communications **71**, 041404 (2005).

[44] J. Jiang, R. Saito, A. Grüneis, S. G. Chou, G. G. Samsonidze, A. Jorio, G. Dresselhaus, and M. S. Dresselhaus, "Intensity of the Resonance Raman Excitation Spectra of Single-Wall Carbon Nanotubes," Phys. Rev. B **71**, 205420 (2005).

[45] K. Sato, R. Saito, J. Jiang, G. Dresselhaus, and M. S. Dresselhaus, "Chirality Dependence of Many Body Effects of Single Wall Carbon Nanotubes," Vib. Spectrosc. **45**, 89 (2007).

[46] V. Barone, J. E. Peralta, and G. E. Scuseria, "Optical Transition in Metallic Single-Walled Carbon Nanotubes," Nano Lett. **5**, 1830 (2005).